FERMI OBSERVATIONS OF HIGH-ENERGY GAMMA-RAY EMISSION FROM GRB 080825C

A. A. ABDO[1,2], M. ACKERMANN[3], K. ASANO[4,5], W. B. ATWOOD[6], M. AXELSSON[7,8], L. BALDINI[9], J. BALLET[10], D. L. BAND[11,12,60], G. BARBIELLINI[13,14], D. BASTIERI[15,16], K. BECHTOL[3], R. BELLAZZINI[9], B. BERENJI[3], P. N. BHAT[17], E. BISSALDI[18], E. D. BLOOM[3], E. BONAMENTE[19,20], A. W. BORGLAND[3], A. BOUVIER[3], J. BREGEON[9], A. BREZ[9], M. S. BRIGGS[17], M. BRIGIDA[21,22], P. BRUEL[23], T. H. BURNETT[24], G. A. CALIANDRO[21,22], R. A. CAMERON[3], P. A. CARAVEO[25], J. M. CASANDJIAN[10], C. CECCHI[19,20], V. CHAPLIN[17], A. CHEKHTMAN[1,26], C. C. CHEUNG[11], J. CHIANG[3], S. CIPRINI[19,20], R. CLAUS[3], J. COHEN-TANUGI[27], L. R. COMINSKY[28], V. CONNAUGHTON[17], J. CONRAD[8,29,30,61], S. CUTINI[31], C. D. DERMER[1], A. DE ANGELIS[32], F. DE PALMA[21,22], S. W. DIGEL[3], E. DO COUTO E SILVA[3], P. S. DRELL[3], R. DUBOIS[3], D. DUMORA[33,34], C. FARNIER[27], C. FAVUZZI[21,22], W. B. FOCKE[3], M. FRAILIS[32], Y. FUKAZAWA[35], P. FUSCO[21,22], F. GARGANO[22], D. GASPARRINI[31], N. GEHRELS[11,36], S. GERMANI[19,20], L. GIBBY[37], B. GIEBELS[23], N. GIGLIETTO[21,22], F. GIORDANO[21,22], T. GLANZMAN[3], G. GODFREY[3], J. GRANOT[38], I. A. GRENIER[10], M.-H. GRONDIN[33,34], J. E. GROVE[1], L. GUILLEMOT[33,34], S. GUIRIEC[17], Y. HANABATA[35], A. K. HARDING[11], M. HAYASHIDA[3], E. HAYS[11], R. E. HUGHES[39], G. JÓHANNESSON[3], A. S. JOHNSON[3], W. N. JOHNSON[1], T. KAMAE[3], H. KATAGIRI[35], J. KATAOKA[4,40], N. KAWAI[4,41], M. KERR[24], J. KNÖDLSEDER[42], D. KOCEVSKI[3], N. KOMIN[10,27], C. KOUVELIOTOU[43], F. KUEHN[39], M. KUSS[9], L. LATRONICO[9], F. LONGO[13,14], F. LOPARCO[21,22], B. LOTT[33,34], M. N. LOVELLETTE[1], P. LUBRANO[19,20], A. MAKEEV[1,26], M. N. MAZZIOTTA[22], S. MCBREEN[18,44], J. E. MCENERY[11], S. MCGLYNN[8,30], C. MEEGAN[45], C. MEURER[8,29], P. F. MICHELSON[3], W. MITTHUMSIRI[3], T. MIZUNO[35], C. MONTE[21,22], M. E. MONZANI[3], E. MORETTI[13,14,46], A. MORSELLI[47], I. V. MOSKALENKO[3], S. MURGIA[3], T. NAKAMORI[4], P. L. NOLAN[3], J. P. NORRIS[48], E. NUSS[27], M. OHNO[49], T. OHSUGI[35], N. OMODEI[9], E. ORLANDO[18], J. F. ORMES[48], M. OZAKI[49], W. S. PACIESAS[17], D. PANEQUE[3], J. H. PANETTA[3], D. PARENT[33,34], V. PELASSA[27], M. PEPE[19,20], M. PESCE-ROLLINS[9], F. PIRON[27], T. A. PORTER[6], R. PREECE[17], S. RAINÒ[21,22], R. RANDO[15,16], M. RAZZANO[9], S. RAZZAQUE[1,2], O. REIMER[3,50], T. REPOSEUR[33,34], S. RITZ[6,11], L. S. ROCHESTER[3], A. Y. RODRIGUEZ[51], M. ROTH[24], F. RYDE[8,30], H. F.-W. SADROZINSKI[6], D. SANCHEZ[23], A. SANDER[39], P. M. SAZ PARKINSON[6], J. D. SCARGLE[52], C. SGRÒ[9], E. J. SISKIND[53], D. A. SMITH[33,34], P. D. SMITH[39], G. SPANDRE[9], P. SPINELLI[21,22], M. STAMATIKOS[11], M. S. STRICKMAN[1], D. J. SUSON[54], H. TAJIMA[3], H. TAKAHASHI[35], T. TANAKA[3], J. B. THAYER[3], J. G. THAYER[3], L. TIBALDO[15,16], D. F. TORRES[51,55], G. TOSTI[19,20], A. TRAMACERE[3,56], Y. UCHIYAMA[3,49], T. L. USHER[3], A. J. VAN DER HORST[43,62], V. VASILEIOU[11,12,57], N. VILCHEZ[42], V. VITALE[47,58], A. VON KIENLIN[18], A. P. WAITE[3], P. WANG[3], C. WILSON-HODGE[43], B. L. WINER[39], K. S. WOOD[1], T. YLINEN[8,30,59], AND M. ZIEGLER[6]

[1] Space Science Division, Naval Research Laboratory, Washington, DC 20375, USA
[2] National Research Council Research Associate, National Academy of Sciences, Washington, DC 20001, USA
[3] W. W. Hansen Experimental Physics Laboratory, Kavli Institute for Particle Astrophysics and Cosmology, Department of Physics and SLAC National Accelerator Laboratory, Stanford University, Stanford, CA 94305, USA; bouvier@stanford.edu
[4] Department of Physics, Tokyo Institute of Technology, Meguro City, Tokyo 152-8551, Japan
[5] Interactive Research Center of Science, Tokyo Institute of Technology, Meguro City, Tokyo 152-8551, Japan
[6] Santa Cruz Institute for Particle Physics, Department of Physics and Department of Astronomy and Astrophysics, University of California at Santa Cruz, Santa Cruz, CA 95064, USA
[7] Department of Astronomy, Stockholm University, SE-106 91 Stockholm, Sweden
[8] The Oskar Klein Centre for Cosmo Particle Physics, AlbaNova, SE-106 91 Stockholm, Sweden
[9] Istituto Nazionale di Fisica Nucleare, Sezione di Pisa, I-56127 Pisa, Italy
[10] Laboratoire AIM, CEA-IRFU/CNRS/Université Paris Diderot, Service d'Astrophysique, CEA Saclay, 91191 Gif sur Yvette, France
[11] NASA Goddard Space Flight Center, Greenbelt, MD 20771, USA
[12] Center for Research and Exploration in Space Science and Technology (CRESST), NASA Goddard Space Flight Center, Greenbelt, MD 20771, USA
[13] Istituto Nazionale di Fisica Nucleare, Sezione di Trieste, I-34127 Trieste, Italy
[14] Dipartimento di Fisica, Università di Trieste, I-34127 Trieste, Italy
[15] Istituto Nazionale di Fisica Nucleare, Sezione di Padova, I-35131 Padova, Italy
[16] Dipartimento di Fisica "G. Galilei," Università di Padova, I-35131 Padova, Italy
[17] University of Alabama in Huntsville, Huntsville, AL 35899, USA
[18] Max-Planck Institut für extraterrestrische Physik, 85748 Garching, Germany
[19] Istituto Nazionale di Fisica Nucleare, Sezione di Perugia, I-06123 Perugia, Italy
[20] Dipartimento di Fisica, Università degli Studi di Perugia, I-06123 Perugia, Italy
[21] Dipartimento di Fisica "M. Merlin" dell'Università e del Politecnico di Bari, I-70126 Bari, Italy
[22] Istituto Nazionale di Fisica Nucleare, Sezione di Bari, 70126 Bari, Italy
[23] Laboratoire Leprince-Ringuet, École polytechnique, CNRS/IN2P3, Palaiseau, France
[24] Department of Physics, University of Washington, Seattle, WA 98195-1560, USA
[25] INAF-Istituto di Astrofisica Spaziale e Fisica Cosmica, I-20133 Milano, Italy
[26] George Mason University, Fairfax, VA 22030, USA
[27] Laboratoire de Physique Théorique et Astroparticules, Université Montpellier 2, CNRS/IN2P3, Montpellier, France
[28] Department of Physics and Astronomy, Sonoma State University, Rohnert Park, CA 94928-3609, USA
[29] Department of Physics, Stockholm University, AlbaNova, SE-106 91 Stockholm, Sweden
[30] Department of Physics, Royal Institute of Technology (KTH), AlbaNova, SE-106 91 Stockholm, Sweden
[31] Agenzia Spaziale Italiana (ASI) Science Data Center, I-00044 Frascati (Roma), Italy
[32] Dipartimento di Fisica, Università di Udine and Istituto Nazionale di Fisica Nucleare, Sezione di Trieste, Gruppo Collegato di Udine, I-33100 Udine, Italy
[33] Université de Bordeaux, Centre d'Études Nucléaires Bordeaux Gradignan, UMR 5797, Gradignan, 33175, France
[34] CNRS/IN2P3, Centre d'Études Nucléaires Bordeaux Gradignan, UMR 5797, Gradignan, 33175, France
[35] Department of Physical Sciences, Hiroshima University, Higashi-Hiroshima, Hiroshima 739-8526, Japan
[36] University of Maryland, College Park, MD 20742, USA
[37] Science Applications International Corporation, Huntsville, AL 35899, USA

[38] Centre for Astrophysics Research, University of Hertfordshire, College Lane, Hatfield AL10 9AB, UK; j.granot@herts.ac.uk
[39] Department of Physics, Center for Cosmology and Astro-Particle Physics, The Ohio State University, Columbus, OH 43210, USA
[40] Waseda University, 1-104 Totsukamachi, Shinjuku-ku, Tokyo, 169-8050, Japan
[41] Cosmic Radiation Laboratory, Institute of Physical and Chemical Research (RIKEN), Wako, Saitama 351-0198, Japan
[42] Centre d'Étude Spatiale des Rayonnements, CNRS/UPS, BP 44346, F-30128 Toulouse Cedex 4, France
[43] NASA Marshall Space Flight Center, Huntsville, AL 35812, USA; Alexander.J.VanDerHorst@nasa.gov
[44] University College Dublin, Belfield, Dublin 4, Ireland
[45] Universities Space Research Association (USRA), Columbia, MD 21044, USA
[46] Istituto Nazionale di Fisica Nucleare, Sezione di Trieste, and Università di Trieste, I-34127 Trieste, Italy
[47] Istituto Nazionale di Fisica Nucleare, Sezione di Roma "Tor Vergata," I-00133 Roma, Italy
[48] Department of Physics and Astronomy, University of Denver, Denver, CO 80208, USA
[49] Institute of Space and Astronautical Science, JAXA, 3-1-1 Yoshinodai, Sagamihara, Kanagawa 229-8510, Japan
[50] Institut für Astro- und Teilchenphysik and Institut für Theoretische Physik, Leopold-Franzens-Universität Innsbruck, A-6020 Innsbruck, Austria
[51] Institut de Ciencies de l'Espai (IEEC-CSIC), Campus UAB, 08193 Barcelona, Spain
[52] Space Sciences Division, NASA Ames Research Center, Moffett Field, CA 94035-1000, USA
[53] NYCB Real-Time Computing Inc., Lattingtown, NY 11560-1025, USA
[54] Department of Chemistry and Physics, Purdue University Calumet, Hammond, IN 46323-2094, USA
[55] Institució Catalana de Recerca i Estudis Avançats, Barcelona, Spain
[56] Consorzio Interuniversitario per la Fisica Spaziale (CIFS), I-10133 Torino, Italy
[57] University of Maryland, Baltimore County, Baltimore, MD 21250, USA
[58] Dipartimento di Fisica, Università di Roma "Tor Vergata," I-00133 Roma, Italy
[59] School of Pure and Applied Natural Sciences, University of Kalmar, SE-391 82 Kalmar, Sweden

ABSTRACT

The *Fermi Gamma-ray Space Telescope* has opened a new high-energy window in the study of gamma-ray bursts (GRBs). Here we present a thorough analysis of GRB 080825C, which triggered the *Fermi* Gamma-ray Burst Monitor (GBM), and was the first firm detection of a GRB by the *Fermi* Large Area Telescope (LAT). We discuss the LAT event selections, background estimation, significance calculations, and localization for *Fermi* GRBs in general and GRB 080825C in particular. We show the results of temporal and time-resolved spectral analysis of the GBM and LAT data. We also present some theoretical interpretation of GRB 080825C observations as well as some common features observed in other LAT GRBs.

Key words: gamma rays: bursts

1. INTRODUCTION

Gamma-ray bursts (GRBs) originate from the most luminous explosions in the universe and more than 35 years after their discovery in 1967 (Klebesadel et al. 1973), many questions remain to be answered about their possible progenitors, the composition of the ultra-relativistic outflows that power them, and the dominant emission mechanism for their prompt gamma rays. The Burst And Transient Source Experiment (BATSE) on board the *Compton Gamma Ray Observatory* (*CGRO*; 1991–2000) made significant advances to the field, thoroughly exploring the 25 keV–2 MeV energy range with detailed population studies of the prompt gamma-ray emission. Burst spectra were found to be well described by the Band function (Band et al. 1993), which consists of two smoothly connected power laws. It was understood, however, that observations of GRBs at higher energies were of crucial importance to resolve some of the open issues: constrain the bulk Lorentz factor of the outflow and the distance from the central source to the gamma-ray emission region, distinguish between hadronic and leptonic origins of the gamma-ray emission, and probe for signatures of Ultra High Energy Cosmic Rays (UHECRs) which could be accelerated within GRB jets (see Band et al. 2009, for a review of the prospects for GRB science with the *Fermi* Large Area Telescope).

Constraints on the origin of the high-energy emission from GRBs are quite limited due to both the small number of bursts with firm high-energy detection and the small number of events that were detected in such cases. High-energy emission from GRBs was first observed by the Energetic Gamma-Ray Experiment Telescope (EGRET; covering the energy range from 30 MeV to 30 GeV) on board *CGRO*. Emission above 100 MeV was detected in five cases: GRBs 910503, 910601, 930131, 940217, and 940301 (Dingus 1995). One of these sources, GRB 930131, had high-energy emission that was consistent with an extrapolation from its spectrum obtained with BATSE between 25 keV and 4 MeV (Sommer et al. 1994). In contrast, evidence for an additional high-energy component up to 200 MeV with a different temporal behavior to the low-energy component was discovered in GRB 941017 (in EGRET's calorimeter, the Total Absorption Shower Counter; Gonzalez et al. 2003). The high-energy emission for the latter GRB lasted more than 200 s with a single spectral component being ruled out. A unique aspect of the high-energy emission in GRB 940217 was its duration, which lasted up to ~90 minutes after the BATSE GRB trigger, including an 18 GeV photon at ~75 minutes post-trigger (Hurley et al. 1994). More recently, the GRID instrument on board *Astro-rivelatore Gamma a Immagini LEggero* (*AGILE*) detected 10 high-energy events with energies up to 300 MeV from GRB 080514B, in coincidence with its lower energy emission, with a significance of 3.0 σ (Giuliani et al. 2008).

The *Fermi Gamma-ray Space Telescope* was launched on 2008 June 11 and provides an unprecedented energy coverage and sensitivity for the study of high-energy emission in GRBs. It is composed of two instruments: the Gamma-ray Burst Monitor (GBM; Meegan et al. 2009) and the Large Area Telescope (LAT;

[60] Deceased
[61] Royal Swedish Academy of Sciences Research Fellow, funded by a grant from the K. A. Wallenberg Foundation.
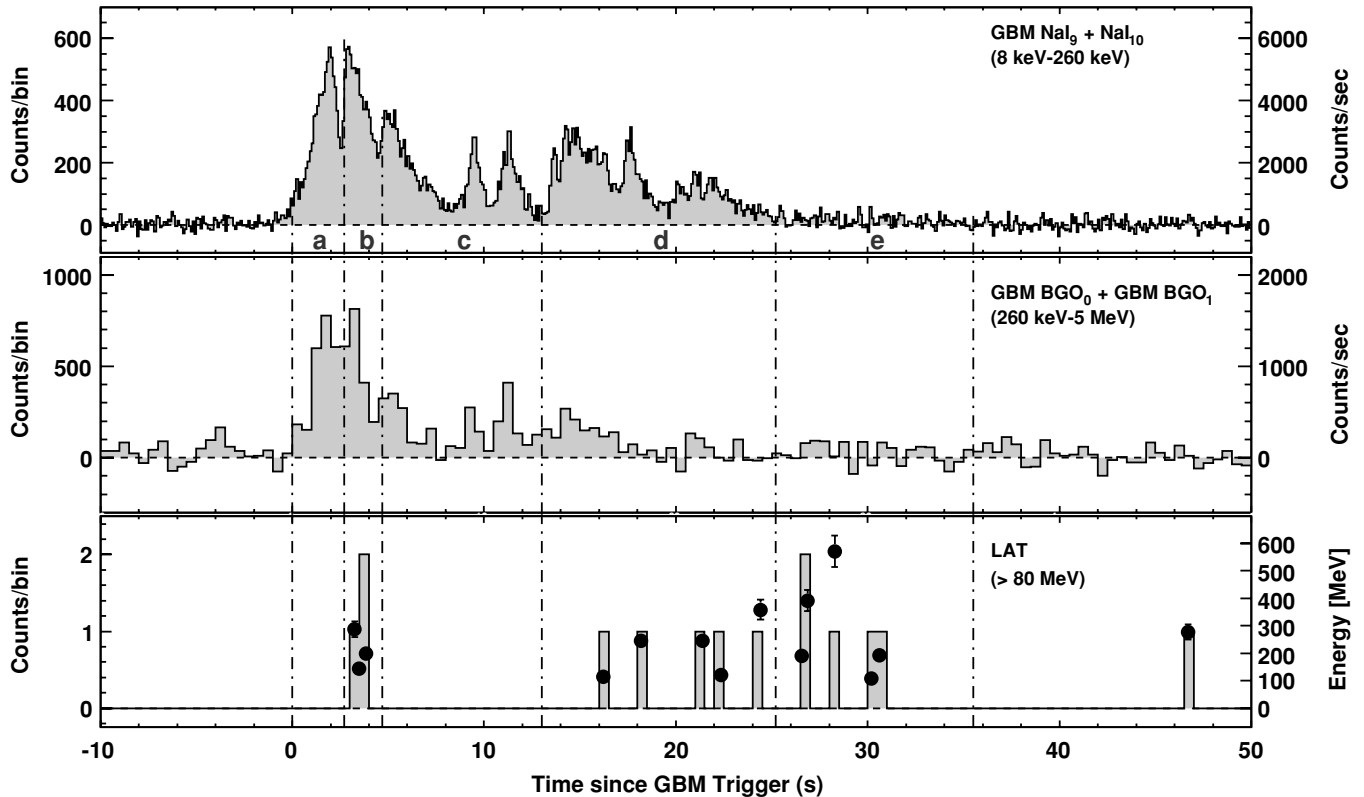[62] NASA Postdoctoral Program Fellow

Figure 1. Light curves of GRB 080825C observed by the GBM (NaI & BGO) and LAT instruments; top two panels are background subtracted. The LAT light curve has been generated using events which passed the "S3" event selection above 80 MeV (which are also the events used for our spectral analysis). Black dots, along with their error bars (systematic uncertainty in the LAT energy measurement) represent the 1σ energy range (right y-axis) for each LAT event. The vertical dash-dotted lines indicate the time bins used in our time-resolved spectral analysis.

Atwood et al. 2009). The GBM covers the entire unocculted sky with 12 sodium iodide (NaI) detectors with different orientation placed around the spacecraft and covering an energy range from 8 keV to 1 MeV, and two bismuth germanate (BGO) scintillators placed on opposite sides of the spacecraft with energy coverage from 200 keV to 40 MeV. The LAT is a pair conversion telescope made up of 4×4 arrays of silicon strip trackers and cesium iodide calorimeter modules covered by a segmented anti-coincidence detector designed to efficiently reject charged particles. The energy coverage of the LAT instrument ranges from 20 MeV to more than 300 GeV with a field of view (FoV) of $\sim$2.4 sr. Note that the LAT effective area is still non-zero even as far out as $70°$ off-axis which allows the detection of bursts with such high incident angles. As of 2009 June 1, nine GRBs have been detected by the LAT at energies above 100 MeV: GRB 080825C (Bouvier et al. 2008), GRB 080916C (Abdo et al. 2009a; Tajima et al. 2008), GRB 081024B (Omodei et al. 2008), GRB 081215A (McEnery et al. 2008), GRB 090217 (Ohno et al. 2009a), GRB 090323 (Ohno et al. 2009b), GRB 090328 (McEnery et al. 2009; Cutini et al. 2009), GRB 090510 (Ohno et al. 2009c; Omodei et al. 2009). In this paper, we report the observations and analyses of gamma-ray emission from GRB 080825C, the first GRB detected by both the GBM and the LAT instruments. Section 2 will present the GBM and LAT observations along with the various methods used for data analysis, Section 3 provides the results of detailed time-resolved spectroscopy, and Section 4 discusses the theoretical interpretation of our observations and compares the properties of this event to the ones observed in some other LAT GRBs.

2. BURST DETECTION AND LOCALIZATION

2.1. GBM Observations

At 14:13:48 UTC on 2008 August 25 (T_0), GRB 080825C triggered the GBM flight software (trigger 241366429, Van der Horst et al. 2008). On-ground analysis of the GBM data localized the burst at right ascension (R.A., J2000) = $232°2$, declination (decl. J2000) = $-4°9$, with a statistical uncertainty of $1°5$ at the 1σ confidence level. The GBM on-ground localization placed this GRB at $\sim60°$ from the LAT boresight at the time of the trigger, at the edge of the LAT FoV, where the effective area is a factor of $\sim$3 less than on axis.

The top two panels of Figure 1 show the background subtracted light curves (see Section 3.2) of the two brightest NaI detectors (9 and 10) and of the two BGO detectors. The GRB exhibits a multiple peak structure with the two brightest peaks seen right after onset. The T_{90} and T_{50} durations of the event (time during which 90% and 50% of the event flux was collected, cf. Kouveliotou et al. 1993) were estimated to be (8–1000 keV) $\sim$27 s and $\sim$13 s, respectively. Emission in the NaI and BGO detectors becomes extremely weak after $\sim T_0 + 25$ s. However, emission is detected in the NaI scintillators up to $\sim$35 s after the trigger time with a 3.6σ significance in bin (e).

2.2. LAT Observations

The LAT events detected close to the GBM position around the trigger time are shown in the bottom panel of Figure 1 (see details below). The LAT data show a count rate increase that

is spatially and temporally correlated with the GBM emission. We have performed a detailed analysis of the significance of this detection. Details on this computation as well as of the LAT data selection, background estimation and localization are given below.

2.2.1. Event Selection

Most of the events detected by the LAT instrument are cosmic rays that need to be distinguished from any source of γ-ray signal. The broad range of LAT observations and analyses, from GRBs to extended diffuse radiation, leads to different optimizations of the event selections which have different rates of residual backgrounds (misclassified cosmic rays). The LAT background rejection analysis has been constructed to allow analysis classes to be optimized for specific science topics (Atwood et al. 2009). In the case of GRB observations, the relatively small region of the sky as well as the very short time window allows the background rejection cuts to be relaxed relative to an analysis of a diffuse source covering a large portion of the sky over longer periods of time. Indeed, the so-called "diffuse" event class is most suited for studying faint sources (like diffuse gamma-ray emission) with minimum background contamination. In the case of GRB 080825C, it was used to search for possible high-energy afterglow emission up to 13 ks after the burst trigger (see Section 3.1.2). On shorter timescales, a significant improvement in the signal-to-noise ratio can be obtained by increasing the effective area while keeping the background rate at a reasonable level. The so-called "transient" event class was developed for this specific purpose and is used for burst detection and localization.

Using Monte Carlo simulations as well as real data input, the event selection used for spectral analysis has been optimized compared to previous analyses (Abdo et al. 2009a) that uses the "transient" class for the prompt emission analysis. Indeed, we found that cuts can be loosened even further for typical burst duration since background contamination is less of an issue for short time windows. For this purpose, a more relaxed event class, so-called "S3," has been developed to improve the LAT effective area at the expense of an increase in the background rate. The pure effective area increase is on the order of $\sim$30 % at 100 MeV and $\sim$10% at 1 GeV. For a typical GRB spectrum, the gamma efficiency above 80 MeV increases by a factor of 20% when using the "S3" class (with a small dependence on spectral index and incidence angle) when the all-sky background rate increases from $\sim$4.2 Hz ("transient") to $\sim$5.2 Hz ("S3"). Our study showed that "S3" brings improvement over the "transient" class in terms of the signal-to-noise ratio (Signal/$\sqrt{\text{Signal} + \text{Background}}$) above 80 MeV. This improvement depends on the brightness of the burst and is of the order of 15% for bursts with GRB 080825C characteristics. As a consequence, the "S3" event class was used for the spectral analysis of GRB 080825C. Note that the lower energy threshold does not add any additional systematics compared to the previously used 100 MeV threshold (see Section 3.2).

Finally, the event selection makes use of the spatial information around the best LAT localization. The LAT point-spread function (PSF) has a strong dependence with energy as well as with the conversion point in the tracker. LAT events are thus separated into FRONT (conversion in the upper part of the tracker) and BACK (conversion in the lower part of the tracker) events (Atwood et al. 2009) for which separate response functions are provided. The region of interest (ROI) considered in this anal-

ysis is energy dependent and based on the 95% containment radius (PSF95) and the 95% LAT error localization (Err95):

$$\text{ROI}(E) = \sqrt{\text{PSF95}(E)^2 + \text{Err95}^2}.$$

To avoid large background contamination, a maximum size is set at 10 and 12 deg for FRONT and BACK events, respectively. In the particular case of GRB 080825C, ROI($E < 200$ MeV) is set to this maximum size and ROI(~ 500 MeV) = 2.9 and 4.0 degrees for FRONT and BACK events, respectively.

All events resulting from this selection process are shown in the bottom panel of Figure 1.

2.2.2. Background Estimation

Since the number of events detected by the LAT is only 15 (of which 13 have an energy $>$80 MeV and can be used for spectral analysis), we need to carefully estimate the expected number of background events in order to calculate the statistical significance of our measurements. The background in the LAT data used for this analysis is dominated by cosmic rays (CRs), with a small contribution from extragalactic and Galactic diffuse gamma rays. Because the earth's limb was $\sim$85° from the GRB location, the contamination from earth-albedo events was negligible and consisted of events with very poorly reconstructed directions. The background rate is a function of many parameters and can vary by more than a factor of 2, depending on the observational conditions. For example, there is a strong dependence of the CR-background rate on the geomagnetic coordinates at the location of the spacecraft. Furthermore, the background rate also depends on the burst position in instrument coordinates, because the LAT's acceptance varies strongly with the inclination angle. For these reasons, it is not straightforward to estimate the expected amount of background during the GRB emission using off-source regions around the trigger time, since the spacecraft will have moved to regions of different geomagnetic coordinates, and the inclination angle of the region of interest will have changed significantly. All these effects are properly taken into account to estimate the background rate for our specific observational conditions. Because the two background components (CRs and gamma rays) have different properties, they are estimated separately using two different methods. The amount of gamma-ray background from some direction in the celestial sphere depends only on the accumulated exposure in that particular direction. Therefore, this component can be estimated by simply scaling the number of gamma rays detected in six months of LAT data, produced during normal science operations, by the ratio of the exposure of the GRB observation over the exposure of the six-month data set. Similar to the above, the amount of CR background from some direction in the celestial sphere depends on the exposure in that direction. However, unlike the above, the CR background also depends on the geomagnetic coordinates at the location of the spacecraft at each instant of the observation. Because of the latter dependence, the CR background cannot be calculated the same way as the gamma-ray background. Instead, a Monte Carlo simulation of the GRB observation is performed, in which parameterizations of the dependence of the CR-background rate on the geomagnetic coordinates and on the inclination angle are used to estimate it for each second of the observation. These two methods will be described in detail below. The CR-background estimation was based on properties of the LAT data extracted from a subset of six months of data selecting when the Galactic plane was far from the center of the

LAT's FoV ($|B| > 70°$). During such observations, and for the transient and S3 data classes, the gamma-ray contribution to the detected signal is negligible, and the detected events can be approximated as being cosmic rays. Specifically, for the transient class, the gamma-ray contamination in this subset of the data is about 10%, which consists of comparable amounts of galactic and extragalactic diffuse emissions and a negligible contribution from resolved point sources. For the S3 class, the gamma-ray contamination is comparable, although slightly lower. After extracting the dependence of the CR-background rate on the geomagnetic coordinates at the position of the spacecraft, we used this dependence to calculate the all-sky CR-background rate for each second of the GRB observation. Then, a corresponding number of simulated events were generated with directions in instrument-centered coordinates, off-axis angle θ, and azimuthal angle ϕ, selected to match the observed distribution in the same subset of the six months of LAT data as used above. These coordinates were then converted to equatorial coordinates, using the instrument's pointing information and were added to a skymap. The simulation procedure described above was repeated hundreds of millions of times. The individual skymaps generated at each one of the iterations were then averaged to obtain a single skymap that showed the expected amount of CR background from each direction of the celestial sphere for the specific GRB observation. As mentioned above, the gamma-ray component of the background was estimated by rescaling the number of gamma rays detected during six months of LAT data (without applying a cut on the galactic latitude of the LAT pointing direction this time). First, a CR-background map corresponding to the six-month period was created by following the procedure mentioned in the previous paragraph. Then, an all-particle (both CRs and gamma rays) map was filled with the directions of all the events actually detected by the LAT during the six-month period. Then, the estimated CR-background map was subtracted from that all-particle six-month map to produce a residual map that was assumed to contain only gamma rays. The number of gamma rays detected during the GRB observation was then calculated by scaling the residual map with the ratio of the exposures of the two periods (six months exposure over GRB-observation exposure). The procedures of estimating the CR and gamma-ray components of the background described above were repeated for 40 different energy ranges spaced logarithmically from 20 MeV to 300 GeV. For each energy range, the CR-background estimations used a different dependence of the CR-background rate on the geomagnetic coordinates, and θ and ϕ distributions. Similarly, the gamma-ray background estimations used different instrument-response functions for the exposure calculations. The resulting CR and gamma-ray maps were then added to produce all-particle estimated background maps (one for each energy range). The new maps were then integrated over the energy-dependent regions of interest to produce the final all-particle background estimates. The all-sky fraction of gamma-rays in the background appears consistent with the $|B| > 70°$ gamma-ray fraction, such that it contributes $\sim 10\%$ toward the overall background rate. The results of this method were tested against actual LAT data for a variety of durations, locations in the celestial sphere, energies, and data classes. All the distributions of the ratios of the estimated over the actually detected signals followed a Gaussian distribution, with width about 15% and center zero (no systematic overestimation or underestimation of the background). This accuracy did not depend on the direction of the region of interest (e.g., its distance from the Galactic plane) and

did not have a strong dependence ($\simeq 5\%$) on the observation's duration.

2.2.3. Significance Calculation

Using the "transient" event selection in an energy-dependent analysis region centered around the GBM best localization and no energy selection, we find 15 events (N_{on}) between T_0 and $T_0 + 35$ s (time interval where we find significant emission in the NaI detectors). From the background estimate (Section 2.2.2), the expected number of counts in the same region and time interval is $B_{est} = 1.3$. The gamma-ray contribution to the background estimate for this particular burst was about 8%. In order to assess carefully the significance of this observation, we have used four independent statistical methods which are described below.

The first method uses an unbinned likelihood analysis of the LAT data which takes into account the energy-dependent PSF in an event-by-event basis. This method finds a significance of 6.5 comparable to the significances found with more simple counting methods described below. This is due to the fact that our selected events have fairly large PSF and thus spatial information within our ROI is not that constraining. In the case of GRBs where high-energy events have been detected, this method is expected to provide the highest significance since it fully takes into account the spatial information for each event.

The second method computes the probability of the null hypothesis being true (the probability that the observed number of counts in the on-source region is due to a background fluctuation) in a frequentist approach that treats the background uncertainty in a semi-Bayesian way (Conrad et al. 2003). Given a certain estimated number of background counts B during the on-source interval, we compute what is the probability of the actual on-source measurement N_{on} being consistent with this value. $P_{sup}(N_{on}, B)$ expresses the probability of the on-source measurement being equal or superior to N_{on} when only statistical fluctuations are considered:

$$P_{sup}(N_{on}, B) = \sum_{N=N_{on}}^{\infty} \frac{e^{-B} \times B^N}{N!}. \tag{1}$$

Because of systematic uncertainties in the background estimation method, each possible value for the number of background counts is weighted using a Gaussian distribution with a mean of B_{est} and a standard deviation of $0.15 \times B_{est}$ (since we estimate our systematics to be about 15%): Gauss (B). We then integrate over all the possible values of B to compute a weighted probability:

$$P_{null} = \frac{\int_0^\infty dB\ \text{Gauss}(B) \times P_{sup}(N_{on}, B)}{\int_0^\infty dB\ \text{Gauss}(B)}. \tag{2}$$

We applied this method for the numbers mentioned above: $N_{on} = 15$ events, $B_{est} = 1.3$, and we obtained a null-hypothesis probability of 1.3×10^{-10}, which corresponds to a significance of 6.6σ.

The third method is fully Bayesian. The question of whether a GRB is detected by the LAT is analyzed as an on-source/off-source observation in the time domain. For the on-source observation, the same parameters are used as in the classical (frequentist) analysis, $T_{on} = 33.0$ s of live time (corresponding to a clock time of 35.5 s) and $N_{on} = 15$. Because the inclination

angle of the best source position with respect to the instrument boresight moved slowly in a 565 s interval around the burst trigger (with $T_{off} = 525.0$ s of live time), we could provide an estimate of the off-source background rate. During this interval, there were $N_{off} = 19$ counts detected, and the corresponding rate is consistent with the previous background estimate B_{est}. The spacecraft motion was favorable for GRB 080825C, allowing an unusually long off-source interval to determine the background rate. For some other GRBs, spacecraft motion may cause the background in the LAT to vary more quickly, limiting the time for which an off-source interval measures the same background as that of the on-source interval, and therefore limiting the applicability of this method.

The Bayesian method assumes that the counts during the background interval are due to a Poissonian process with rate b. To evaluate the probability that a source has been detected during the on-source interval, the method compares two hypotheses for the Poisson rate during the on-source interval: that observed counts are due to the same background rate b, or that they are due to a background plus source rate $b+s$. This second hypothesis is insufficiently specified to quantitatively solve the problem: one must specify some plausible range for the source rate s using prior data (i.e., not using the LAT observations). We produce a reasonable estimate for the LAT source counts by extrapolating the time-integrated spectral fit of the GBM data to the LAT energy range. The photon model from the GBM fit is propagated through the LAT response to predict the number of LAT counts. A real LAT observation could have a smaller value than this estimate because of a statistical fluctuation, or because of a spectral break between the GBM and LAT energy range. Alternatively, a real LAT observation could actually exceed this estimate for the maximum rate if there were an additional and distinct spectral component to the one found with the GBM data alone. Nevertheless, this is a reasonable "prior" estimate for the maximum counts expected in the LAT, which for GRB 082525C is ~60 counts. Under the assumptions described, both Loredo ([1992](#)) and Gregory ([2005](#)) give analytic solutions for the probability P that the source is detected. Using the observational parameters listed above, we find $1 - P = 1.2 \times 10^{-8}$ which corresponds to a 5.6σ significance. Moreover, this method can provide the probabilities for the number of events actually originating from the source: all 15 events (30%), 14 events (35%), 13 events (22%), 12 events (9%), 11 events (3%), $\leqslant 10$ events (1%).

Finally, we have computed the significance with a fully frequentist method using the on-source/off-source approach as described by Li & Ma ([1983](#), Equation (17)). This method yields a significance of 6.4σ for the detecting this burst.

It should be noted that because such search for LAT excess is performed on all GRBs triggered by the GBM and other instruments (when the burst is in the LAT FoV), it is important to consider multi-trials in our analysis. For independent searches as is the case here, the post-trials probability threshold for obtaining a 5σ result is $P_{post-trial} = 1 - (1 - P_{5\sigma})^{1/N}$, where N is the number of trials and $P_{5\sigma}$ the 5σ probability threshold for a single search ($\sim 5.7 \times 10^{-7}$). In the case of GRB 080825C, we searched for LAT excess in ~50 bursts triggered by the GBM which corresponds to a post-trial probability for a 5σ results of $P_{5\sigma, post-trial} \sim 1.15 \times 10^{-8}$. This corresponds to a significance of 5.7 which is therefore our threshold for a 5σ detection.

The four independent significance computations presented above all yield consistent results similar or above this threshold.
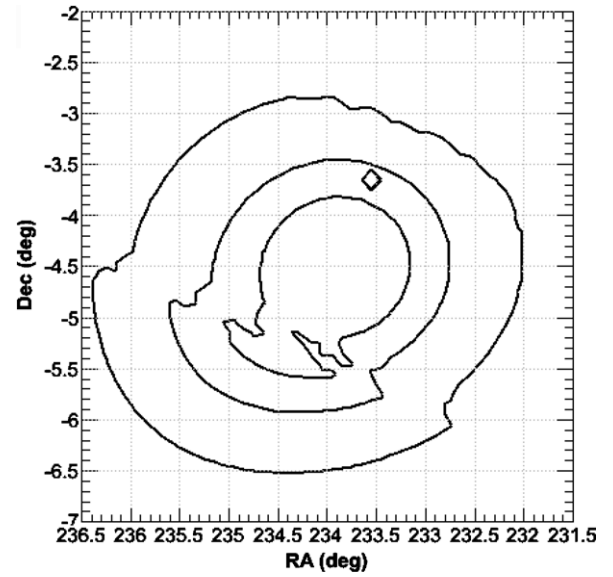

Figure 2. LAT on-ground localization for GRB 080825C: R.A. = 233.9, decl. = −4.5. The contours show the containment regions for confidence levels: 68%, 90%, and 99%. Equivalent containment radii can be computed: 0°.8 (68%), 1°.3 (90%), and 2°.0 (99%).

GRB 080825C is therefore the first GRB detected by the LAT instrument (Bouvier et al. [2008](#)) at a high significance level.

2.2.4. Localization

Due to the strong variation of the LAT PSF with photon energy (Atwood et al. [2009](#)), the on-ground localization of a source depends strongly on its spectral shape. For example, 10 photons detected at 100 MeV will yield an accuracy of ~1°, while one single photon with an energy of 10 GeV will increase the accuracy to $\sim 0°.1$.

The on-ground localization procedure makes use of the "transient" class events. It is restricted to the events detected above 100 MeV (which have a good PSF) in a 15° region around the GBM trigger position (R.A. = 232.2, decl. = −4.9). The method is based on a likelihood ratio test, following the same steps as Mattox et al. ([1996](#)). While these authors used a binned likelihood for the analysis of EGRET data, our likelihood function is unbinned and uses the instrument PSF on an event basis. It also takes into account the various residual backgrounds. First, the position of the source and its spectrum are left free in the fit, assuming a power-law shape. Then, in order to compute an accurate localization error, the test statistics (TS, see Section [3.1.2](#) for a complete definition) of the point source spectral fit is computed at each node of a fine map (5° × 5° for this case, with a bin size of 0°.1). Following Mattox et al. ([1996](#)), the TS values are interpreted in terms of the χ^2 distribution with 2 degrees of freedom (the two map coordinates). Figure [2](#) shows the obtained error contours around the fitted position R.A. = 233.9, decl. = −4.5, with a 68%, 90%, and 99% statistical error radius of 0°.8, 1°.3 and 2°.0, respectively.

At large inclination angles, the systematic error of a source localization with the LAT is dominated by the slight bias in direction reconstruction of low-energy photons. This bias is mainly caused by a trigger effect, which selects those events that scatter downward and interact with at least three tracker planes, as required by the instrument trigger logic (Atwood et al. [2009](#)). The bias is amplified by the reconstruction efficiency, which is larger for tracks near normal incidence. Since the PSF is
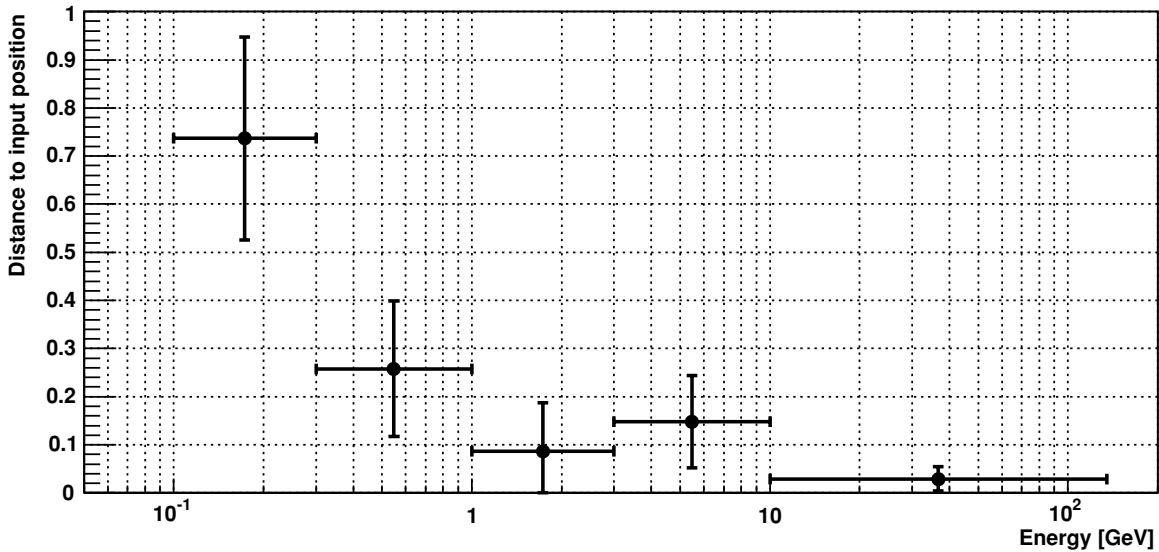
Figure 3. Dependence of the localization bias on the energy range of the events used. These results are obtained from a simulation of LAT observations of a point source similar to GRB 080916C (same slope and inclination angle). The use of low-energy events only (below 1 GeV) yields a noticeable bias, while no bias is seen when using events only above 1 GeV.

assumed to be centered on average on the true directions of the gamma rays, this effect translates to a bias in the fitted position toward a smaller inclination angle.

This systematic error has been evaluated in two steps, using both data and Monte Carlo simulations. In the first step, we studied the LAT performance in localizing the Vela pulsar, which is the brightest source and has a well-determined position from observations at other wavelengths. We found that the fitted position obtained from observations where this source was seen at large inclination angles is biased toward smaller angles. This bias is noticeable only when low-energy events (below 1 GeV) are used, and it disappears when high-energy events (above 1 GeV) are included in the analysis. The agreement found with the prediction of the Monte Carlo simulation allows us to evaluate the bias for any burst observation. For instance, Figure 3 shows how the bias varies with energy range for a bright gamma-ray point source with the same spectral index and inclination angle as GRB 080916C (Abdo et al. 2009a).

In the second step, we used the Monte Carlo simulation to evaluate the localization systematic error for GRB 080825C. We produced a simulation of a point source with the same spectral index (~ -2.3) and inclination angle as GRB 080825C ($\sim 60°$). The position obtained with events between 100 MeV and 570 MeV showed a deviation of $\sim 0°\!.6$ with respect to the input position. This systematic error is larger than the one derived for the very bright GRB 080916C ($\lesssim 0°\!.1$) because GRB 080825C occurred at a larger inclination angle and had a maximum photon energy well below 1 GeV.

3. DATA ANALYSIS

3.1. Temporal Analysis

3.1.1. GBM and LAT Light Curves

The NaI, BGO, and LAT ("S3" selection) light curves are shown in Figure 1. No LAT event is seen in coincidence with the first bright GBM peak. The first three LAT events above 80 MeV are detected in a very short time window, a few seconds after the GBM trigger, in coincidence with the second GBM peak. After a quiet period where no LAT events are detected up

to ~ 16 s, four more events are detected within the GBM T_{90}, and another four events after T_{90} when the NaI emission has faded close to the background level. Interestingly the highest energy event, with an energy of 572 ± 58 MeV, is detected at $\sim T_0 + 28$ s.

To quantify the different features of this GRB (LAT delay, gap, and extended emission), we have performed Monte Carlo simulations of the LAT light curve and estimated the fraction of those simulations that reproduce these features. The LAT event distribution was produced using Poisson statistics for a constant background rate of 0.037 Hz (see Section 2.2.2), an estimated detected signal above 80 MeV of 11.7 events (13 events minus 1.3 estimated background events) and a temporal probability distribution based on the NaI light curve from T_0 to $T_0 + 35$ s. The probability of the different features was computed as follows.

1. *Delay.* The fraction of simulated light curves where the first event arrives later than the first actual observed photon (at $T_0 + 3.252$ s).
2. *Gap.* The fraction of simulated light curves which include a gap in the middle of the light curve with a width larger than the 12.38 s observed.
3. *Extended emission.* The fraction of simulated light curves where the last five events are detected after the timing of the ninth observed event (detected at $T_0 + 26.570$ s).

This analysis finds weak evidence for the possible delay or gap features (with chance probabilities of 3.4% and 0.89%, respectively), but the evidence for temporally extended emission in the LAT is more significant, at a 3.7σ level.

3.1.2. High-energy Afterglow Search

We searched for possible afterglow emission up to 13 ks after the trigger time, but did not find any significant emission. Note that the LAT event detected around $T_0 + 47$ s is consistent with the expected background event every ~ 30 s in the region of interest.

For the search, we selected the time intervals in which the $10°$ region of interest centered on the LAT location (see Section 2.2.4) was in the LAT FoV. The burst location exited
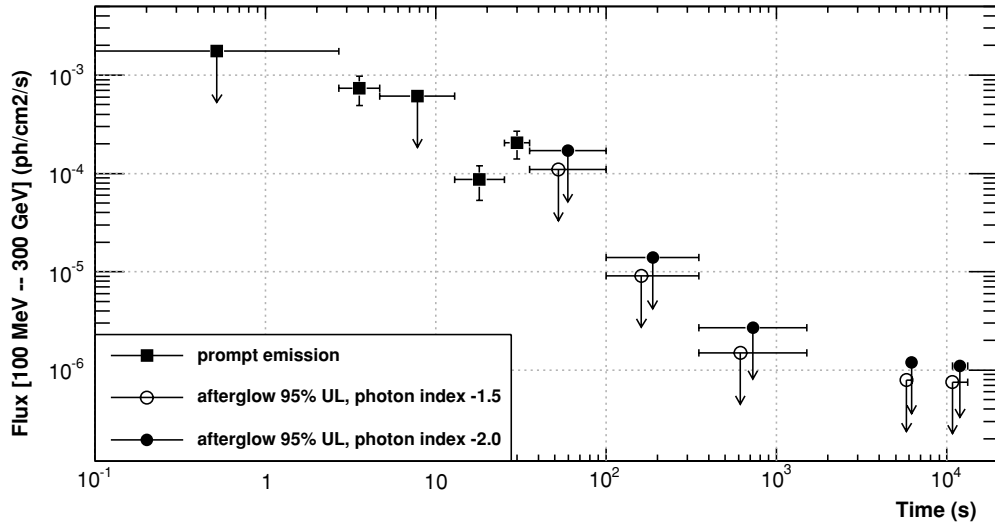
Figure 4. Squares: photon fluxes (or 95 % C.L. upper limits) measured during the prompt emission, in the five time bins defined previously. Filled circles (resp. open circles): 95% C.L. upper limits on the afterglow emission photon flux in each considered time bin, assuming a power-law spectral shape of index −2.0 (resp. −1.5).

the FoV 1500 s after the trigger time, re-entered it ∼1 hr later (at $T_0 + 5200$ s) for ∼1600 s, and again ∼1.5 hr later (at $T_0 + 10800$ s) for ∼2400 s.

These periods were split into five time bins with roughly exponentially increasing durations : 35.5 s–100 s after the trigger time (just at the end of the prompt emission), 100 s–350 s, 350 s–1500 s, 5200 s–6800 s and finally 10800 s–3200 s after the trigger time. We used the "diffuse" event selection (Atwood et al. 2009), which is adapted to faint source studies.

In each time bin, we computed the TS of a point source with a power-law spectrum located at the position of the burst. Two spectral fits were performed using the unbinned maximum likelihood method, one including only background components (the null hypothesis), the other also including a test point source (the alternative hypothesis), with two possible spectral indices: −2.0 (close to the spectral index of the prompt emission in the last time bin) and −1.5 (i.e., a harder spectrum which could arise from an additional spectral component at later times). The Galactic diffuse emission, the isotropic diffuse emission (as described in A. A. Abdo et al. (2009, in preparation), and two likely blazars close to the burst location (0FGL J1511.2−0536 and 0FGL J1512.7−0905; Abdo et al. 2009b) were included in the background model, and their contribution was estimated using pre-burst data for the region of interest. The TS, which is defined as 2 times the difference of the log-likelihoods between the alternative hypothesis and the null hypothesis, was derived in each time bin and for each considered spectral index. All TS values are very close to zero, indicating a null detection.

Since no significant afterglow emission was found, 95% C.L. upper limits on the flux of the possible emission were derived, using a Bayesian method with flat prior (Helene 1983). This method was preferred to the likelihood profile (Rolke at al. 2005) because of the very low count regime. Since the TS is close to zero, the profile is not a symmetric parabola and the upper limits derived by the likelihood profile method do not have proper statistical coverage. The results obtained with the Bayesian method are shown in Figure 4 and in Table 1 for both assumed spectral indices. The upper limit found in the first bin is of the same order of magnitude as the flux derived at the end of the prompt emission. Then the upper limit decreases when the considered observation time increases.

Table 1
95% C.L. Upper Limit on the Photon Flux in the LAT Energy Range Derived by a Bayesian Method with a Flat Prior

Time Bins (s)	Spectral Index	Photon Flux Above 100 MeV 95% C.L. Upper Limit (10^{-6} ph cm^{-2} s^{-1})
a : 0.00–2.69	−2.54	1750
c : 4.74–12.93	−2.62	610
f : 35.5–100.	−2.0/−1.5	170/110
g : 100.–350.	−2.0/−1.5	14/9.1
h : 350.–1500.	−2.0/−1.5	2.7/1.5
i : 5200.–6800.	−2.0/−1.5	1.2/0.79
j : 10800.–13200.	−2.0/−1.5	1.1/0.75

Notes. In time bins (a) and (c) of the prompt emission the continuation of the spectrum fitted on GBM data was assumed. In time bins (f)–(j) two different cases were studied: a spectral index of −2.0 (close to the spectral index of the prompt emission in the last time bin) and of −1.5 (i.e., a harder spectrum which could arise from an additional spectral component at later times).

The same method was used to derive 95% C.L. upper limits on the flux in the prompt emission phase where the LAT did not detect any photon (time bins (a) and (c)). We assumed a spectral index extrapolating the GBM spectrum. These results are shown in Figure 4 and Table 1 as well.

Between bins (e) and (h) we assumed that the flux decreases with time like t^a. We used the fitted flux values on each time bin, and for bins with TS zero, we set the flux to an arbitrary low value (this choice has no impact on the following result). The 68% C.L. error bars were determined by the likelihood profile method. Although its coverage is not correct for the bins of TS zero, this error bar is accurate enough for the present purpose of fitting the flux decay. It also ensures homogeneity among the error bars used for the fit. Since the fitted decay slope was not significant, we used a χ^2 profile method (Rolke at al. 2005) to derive upper limits on the flux decay slope for both assumed spectral indices : $a < -2.08$ (95% C.L.) for a spectral index of −1.5 and $a < -1.77$ (95% C.L.) for a spectral index of −2.0.

3.2. Time-resolved Spectroscopy

We have performed detailed spectroscopy of the combined GBM and LAT data, for the whole duration of the burst and

Table 2
Time-integrated and Time-resolved Spectral Analysis Results for GRB 080825C

Time Range (s)	A (10^{-3} γ cm^{-2} s^{-1} keV^{-1})	α	β	E_{peak} (keV)
a: 0.00–2.69	75^{+6}_{-5}	-0.76 ± 0.05	$-2.54^{+0.11}_{-0.17}$	291^{+25}_{-22}
b: 2.69–4.74	138^{+13}_{-11}	-0.52 ± 0.06	$-2.37^{+0.06}_{-0.08}$	210^{+14}_{-12}
c: 4.74–12.93	44 ± 4	-0.81 ± 0.06	$-2.62^{+0.14}_{-0.25}$	183 ± 13
d: 12.93–25.22	47^{+5}_{-4}	$-0.72^{+0.07}_{-0.06}$	$-2.45^{+0.07}_{-0.10}$	152 ± 9
e: 25.22–35.46	1.2 ± 0.1 (at 100 keV)	N.A.	-1.95 ± 0.05	N.A.
0.00–35.46	37 ± 2	-0.79 ± 0.03	$-2.42^{+0.04}_{-0.05}$	198 ± 8

Note. Band function best-fit parameters are provided for all spectra, except for time interval (e) which is adequately fit by a single power law.

Table 3
Flux and Fluence in the 50–300 keV and 100–600 MeV Energy Ranges for the Time Intervals and Spectral Parameters Presented in Table 2

Time Bin	Flux$_{50-300\,\text{keV}}$ (10^{-7} erg s^{-1} cm^{-2})	Flux$_{100-600\,\text{MeV}}$ (10^{-8} erg s^{-1} cm^{-2})	Fluence$_{50-300\,\text{keV}}$ (10^{-6} erg cm^{-2})	Fluence$_{100-600\,\text{MeV}}$ (10^{-7} erg cm^{-2})
a	16.2 ± 0.2	< 20.1	4.35 ± 0.05	< 5.39
b	20.9 ± 0.3	21.1 ± 7.2	4.28 ± 0.06	4.32 ± 1.47
c	6.57 ± 0.11	< 3.78	5.38 ± 0.09	< 3.09
d	5.50 ± 0.07	2.50 ± 0.97	6.76 ± 0.09	3.07 ± 1.19
e	0.34 ± 0.03	5.03 ± 1.68	0.35 ± 0.03	5.15 ± 1.72
Full	5.98 ± 0.04	4.35 ± 0.88	21.2 ± 0.1	15.4 ± 3.1

Note. The upper limits are given at the 2σ level.

also time-resolved analysis based on the temporal structures observed in the GBM and LAT light curves. Figure 1 shows the five time intervals ((a)–(e)) adopted for this analysis. The fits were performed with the spectral analysis software package RMFIT (version 2.5), using log-likelihood as the fitting statistic since chi-squared is less appropriate due to the low number of events at high gamma-ray energies in this burst. The variable GBM background is subtracted for all detectors individually by fitting an energy-dependent, second-order polynomial to background data of ∼300 s before and ∼300 s after the GRB. For the LAT data, the "S3" event selection is used (see Section 2.2.1). We used a LAT energy range from 80 MeV to 200 GeV (since energy bins with no detection still contain useful information) and adopted a constant but energy-dependent background rate, as described in Section 2.2.2. For the GBM data, we used the standard 128 energy bins of the CSPEC data-type, but only the channels above 8 keV in the NaI detectors, above 240 keV in the BGO detectors, and rejecting the overflow channels in both NaIs and BGOs.

We considered different empirical models in the spectral analysis: a simple power law, a power law with a high-energy exponential cutoff, a Band function (Band et al. 1993) which smoothly connects two power laws, a Band function with a high-energy exponential cutoff, and a Band function with an additional power law. The high-energy exponential cutoff was implemented by multiplying the original spectrum by $\exp(-E/E_{\text{cutoff}})$. The main results of our combined GBM and LAT analysis are shown in Tables 2 (spectral parameters) and 3 (flux and fluence in 50–300 keV and 100–600 MeV), for which we used the LAT data and responses obtained with the "S3" cut. The time-integrated spectrum (shown in Figure 5) and the time bins (b)–(d) are best fit to a significant degree by the Band function, and thus only the best-fit parameters and associated statistical uncertainties of the Band function are provided in

Table 2 for these time bins. The best-fit parameters for the Band function are also given for time bin (a), although an addition of a possible exponential cutoff is discussed later in this section. For time interval (e), however, the spectrum is adequately described by a single power law, and adding more parameters does not improve the fit. Adding a power-law function to the Band function does not improve the time-integrated and time-resolved fits. Besides spectral fits to the whole GBM & LAT energy range, we also fitted the GBM data alone and propagated the photon model from the GBM fit through the LAT response to obtain the predicted numbers of LAT counts. A comparison between the expected and observed numbers of events shows that there is no need for an extra emission component besides the Band function (or power law for time bin (e)).

Time bins (a)–(d) display the typical hard-to-soft evolution of E_{peak} (Norris et al. 1986), which is the energy at which the Band function peaks in νF_ν spectrum, starting at almost 300 keV and decreasing to ∼150 keV. Except for the second interval, the values of the low-energy spectral index, α, and the high-energy spectral index, β, are constant within their uncertainties. The evolution of the spectral parameters, flux, fluence, and the flux ratio between the two energy ranges are shown in Figure 6. The best-fit model spectra for time bins (a)–(e) are shown in Figure 7 along with their 1σ confidence intervals.

A significant hardening of the spectrum at high energy is observed after ∼25 s. From the light curves (Figure 1), it is clear that while the GBM emission in time bin (e) is just above the background level, there is significant emission in the LAT, including the two highest energy events detected for this GRB. This spectral hardening is also reflected in the power-law index of -1.95 ± 0.05 for time bin (e) (see Table 2), which is significantly harder than the values of β in the earlier time bins. Looking at the evolution of E_{peak}, one could argue that the spectrum is affected by curvature at the low-energy end
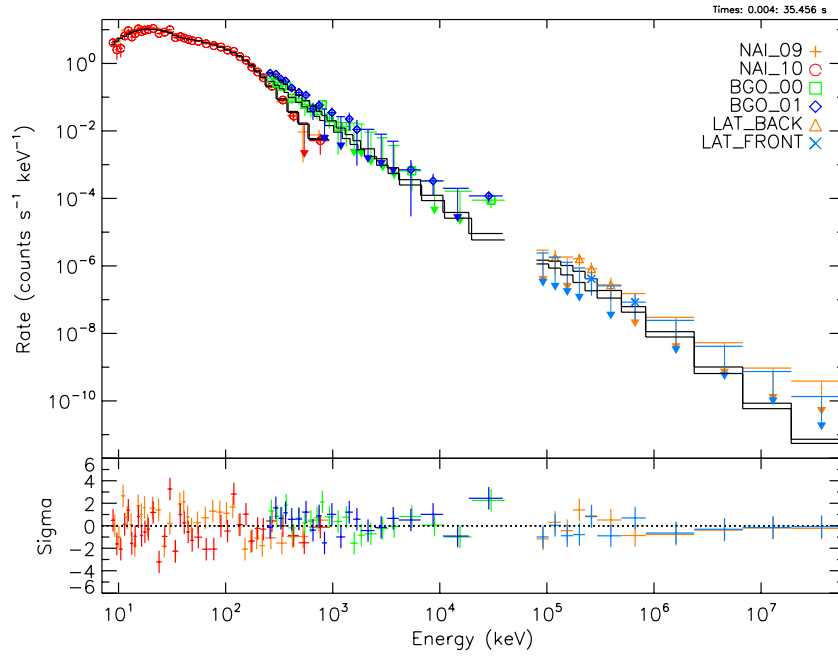
Figure 5. Time-integrated ($T_0 + 0.004$ to $T_0 + 35.456$ s) count spectrum of GRB 080825C of the GBM (NaI and BGO) and LAT data. The spectrum is well fit by a Band function spanning ∼five decades of energy. LAT data have been separated into "FRONT" and "BACK" data sets which, respectively, correspond to events converted in the upper and lower part of the tracker instrument (Atwood et al. 2009).
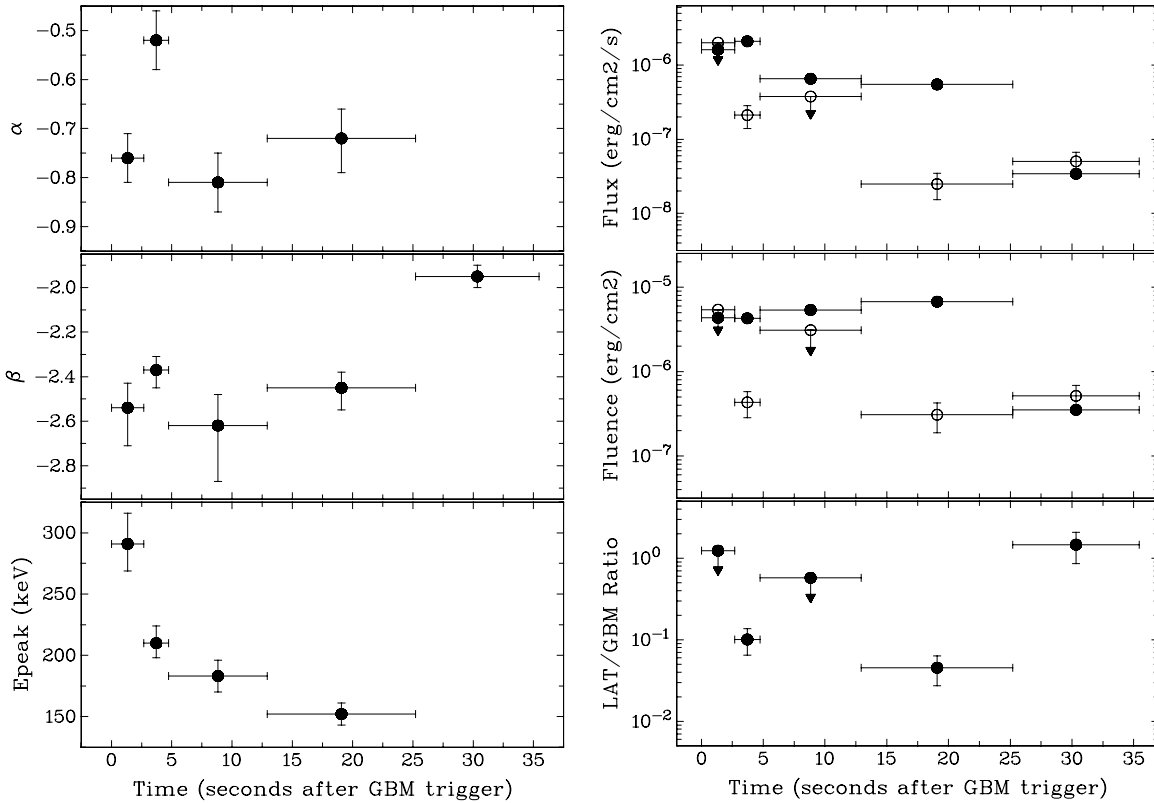

Figure 6. Left: temporal evolution of the spectral parameters for GRB 080825C: the low-energy index α (top), the high-energy index β (middle), and the peak energy E_{peak} (bottom). The last time bin is adequately fit by a single power-law function, of which the index is plotted in the middle panel. Right: temporal evolution of the flux (top) and fluence (middle) in two energy ranges: 50–300 keV (solid circles) and 100–600 MeV (open circles); and of the ratio (bottom) between the high-energy and low-energy flux. The upper limits are given at the 2σ level.

and that a Band function is not preferred over a single power law due to poor statistics. However, a spectral fit in interval (e) of all the data above 300 keV gives a softer but consistent power-law index of -2.10 ± 0.08. This β-value is closer to

the β-values found for interval (a)–(d), but still significantly harder.

We have searched for possible departures from a simple Band function in the different time bins by performing a

Table 4
Systematic Uncertainties as well as the Predominant Effect for Each Spectral Parameter of the Time-integrated Best-fit Band Function Reported in Table 2

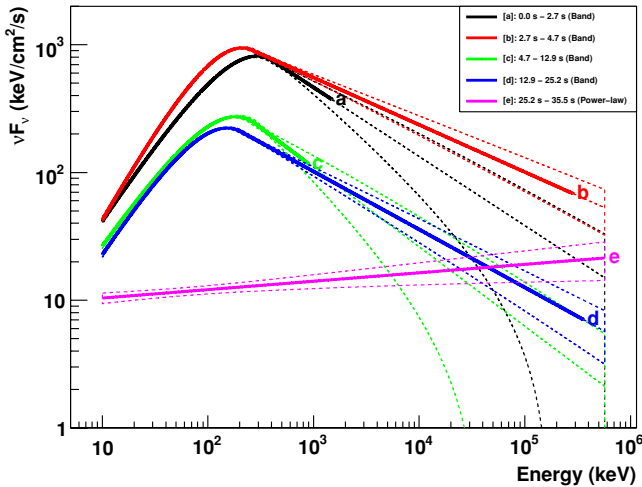| Systematics	Norm	α	β	$E_{\rm peak}$ (keV)
Error	±15%	±0.03	±0.03	±8
Dominant Effect	NaI eff. area	NaI eff. area	BGO eff. area	NaI & BGO eff. area

Figure 7. Best-fit spectra for time bins (a)–(e) are shown in thick solid lines that reach up to the largest detected photon energy in each time bin, while the corresponding (same color) thin dashed lines represent the 1σ confidence contours for each fit. Time bins (a)–(d) are fit by a Band function, and time bin (e) is fit by a power-law spectral model.

likelihood ratio test comparing a simple Band function with a Band function multiplied by an exponential cutoff term, $\exp(-E/E_{\rm cutoff})$. A significance of 4.3σ was found for an exponential cutoff in time bin (a) with a cutoff energy around $E_{\rm cutoff} = 1.77^{+1.59}_{-0.56}$ MeV (with the following Band function parameters: $\alpha \sim -0.57$, $\beta \sim -1.64$, $E_{\rm peak} \sim 211$ keV). We investigated the dependence of this significance with the systematics of our instruments and found the strongest effect to be a $\pm 15\%$ variation in the BGO effective area which can bring the significance down to $\sim 3.7\sigma$. With five time bins, this is not strong enough to claim the existence of an exponential cutoff.

We have performed a careful investigation of the effect of systematic uncertainties on the spectral parameters of GRB 080825C. We considered the following systematics in the LAT, BGO, and NaI detectors: effective area, energy dispersion, and background subtraction. For the LAT, the methodology we use is to modify the Instrument Response Functions (IRFs) in order to take into account those various effects. Systematics on the LAT effective area have been derived from a study of the Vela pulsar and Earth albedo photons because it is possible in both cases to extract an extremely pure gamma-ray sample. Using this sample, the uncertainty on the LAT effective area has been computed as a function of energy to be 10% below 100 MeV, 5% around 1 GeV, and 20% above 10 GeV. Based on this estimate, some special IRFs have been created to encompass the extreme scenarios in overall normalization and slope of the LAT effective area. The uncertainty in energy measurement for the LAT is estimated to be of the order of 5%. We adopted a 10% uncertainty in the NaI and BGO effective area (both overall normalization and slope). Finally, we also considered the uncertainty in the choice of off-timing sample for NaI and BGO background subtraction and found the corresponding systematics to be negligible. In each time bin, the error values on the spectral parameters are found to be similar to or smaller than the statistical uncertainties

reported in Table 2, except for the case of time bins (a) and (b) where the systematics on $E_{\rm peak}$ and the normalization are found to be about 2 times and 3 times larger, respectively. Table 4 reports the systematics found for each parameter of the time-integrated best-fit Band function reported in Table 2 as well as the predominant systematic effects. We note that similar trends for the systematic uncertainties were found for GRB 080916C (Abdo et al. 2009a), which had many more LAT events than GRB 080825C.

4. DISCUSSION

4.1. Theoretical Interpretation of GRB 080825C Observations

GRB 080825C is the first GRB detected by the *Fermi* LAT. Furthermore, it is the first GRB to show a hint of a time delay between the onset of the high-energy (>100 MeV) emission relative to the low-energy (sub-MeV) emission (later seen much more clearly in GRB 080916C; Abdo et al. 2009a). Moreover, there appears to be a local minimum in the high-energy flux between the initial narrow (< 1 s) LAT spike, at ~ 3–4 s after the GBM trigger, and the later, much broader peak (between ~ 16 s and ~ 31 s). GRB 080825C is the first GRB to show this possible feature in the high-energy emission.

The late broad peak in the high-energy emission has a duration comparable to its peak time as measured from the GRB trigger time, and these two timescales are also similar to the duration of the low-energy emission (which has $T_{90} \sim 27$ s and $T_{50} \sim 13$ s). The fact that these three timescales are comparable is naturally accounted for if this late broad peak signifies the onset of the emission from the external (reverse or forward) shocks, if the reverse shock is (at least mildly) relativistic (see Figure 1 of Sari 1997). This occurs around the deceleration time, as the GRB outflow is decelerated by a reverse shock while it drives a highly-relativistic forward shock into the external medium. In this scenario, the late broad LAT peak can be either synchrotron self-Compton (SSC) emission from the reverse shock or external-Compton (EC) emission from the forward-reverse shock system that forms as the GRB outflow is decelerated by the external medium (as was suggested for GRB 941017; Granot & Guetta 2003; Pe'er & Waxman 2004). In the latter case, the seed synchrotron photons can come from the reverse shock and the upscattering relativistic electrons from the forward shock, or vice versa (Wang et al. 2001).

In time bin (e), which contains the second half of the broad high-energy LAT peak while the GBM emission is almost back to background, the spectrum is well fit by a single power law with a photon index of -1.95 ± 0.05, which is significantly harder than the values of the high-energy photon index β in all of the earlier time bins. Moreover, the two highest energy photons in this GRB are in time bin (e). This may suggest that the late time wide high-energy peak arises from a separate spectral component to that responsible for the low-energy emission, which is consistent with an origin from a distinct physical region (and in particular with an external shock origin, as mentioned above). If there is still some contribution from the low-energy spectral component, then the photon index of the high-energy spectral component, which dominates in time bin (e) but is

sub-dominant earlier on, could be somewhat harder than the measured value. A rather flat νF_ν spectrum around ~ 100 MeV might suggest that the peak photon energy of this spectral component is close to this energy range, which may be readily obtained for SSC from the reverse shock, and possibly for the EC process described above. Such a spectrum would disfavor SSC from the forward shock, which typically peaks at TeV energies near the deceleration time (Wang et al. 2001; Granot & Guetta 2003; Pe'er & Waxman 2004).

The rate of the rise in flux up to the wide peak is hard to quantify, and therefore does not significantly constrain the theoretical models. The upper limits on the late time high-energy flux imply a flux decay at least as steep as $\sim t^{-1.7}$. This is consistent with the steep decay that is expected from the reverse shock emission after the passage of the reverse shock, but only barely consistent with forward shock SSC emission (e.g., Sari & Esin 2001) for fast cooling for a sufficiently soft electron energy distribution, corresponding to a power-law index of $p \gtrsim 2.6$–2.7. Other emission mechanisms might also be able to produce a sufficiently steep flux decay rate.

The possible high-energy cutoff around $E_{\rm cutoff} \sim 1.8$ MeV in time bin (a), i.e., the first 2.7 s from the trigger time, if true, is very interesting, as it does not appear to have a good simple explanation. The lack of a redshift measurement for GRB 080825C, however, makes it difficult to draw very strong conclusions, even in this case. In time bin (a), $E_{\rm peak} \approx 290$ keV is a factor of ~ 6 lower than $E_{\rm cutoff}$, thus disfavoring a quasi-thermal spectrum. A possible origin of such a cutoff from intrinsic opacity to pair production in the source (e.g., Lithwick & Sari 2001; Baring 2006; Granot et al. 2008) might be hard to reconcile with the non-thermal spectrum and sharp peak in the GBM light curve in time bin (a), which both imply that the Thomson optical depth τ_T of the pairs produced in the source cannot be $\gg 1$, for any reasonable redshift (that is not $\ll 1$). Such a reasonable redshift would, in turn, typically imply a bulk Lorentz factor of the emitting region of $\Gamma \gtrsim 100$, and make it very difficult to produce $E_{\rm cutoff} \sim 1.8$ MeV, corresponding to a comoving energy of $E'_{\rm cutoff} \sim 18(1+z)(\Gamma/100)^{-1}$ keV $\ll m_e c^2$. This can be understood as follows. Producing the observed cutoff through intrinsic opacity to pair production requires $\tau_{\gamma\gamma}(E'_{\rm cutoff}) \approx 1$. Since the opacity to pair production for a photon of energy $E'_{\rm cutoff}$ is produced mainly by photons of energy $\sim E'_{\rm an} \sim (m_e c^2)^2/E'_{\rm cutoff}$ (i.e., near threshold), and the cross section to pair production near threshold is of the order of the Thomson cross section (σ_T), then $\tau_{\gamma\gamma}(E') \sim \tau_T [(m_e c^2)^2/E']$, where $\tau_T(E')$ is the Thomson optical depth of the pairs that are produced if all the photons of energy near or above E' pair produce. In particular, taking $E' = E'_{\rm cutoff}$ implies that $\tau_T(E'_{\rm an}) \sim 1$ (i.e., the Thomson optical depth of the pairs produced by all the photons of energy $E' \gtrsim E'_{\rm an}$ is of order unity). In our scenario, $\tau_{\gamma\gamma}(E'_{\rm cutoff}) \approx 1$ implies that all photons above $E'_{\rm cutoff}$ pair produce, and since they are much more numerous than the photons above $E'_{\rm an}$ this produces a very large Thomson optical depth in pairs, $\tau_T(E'_{\rm cutoff}) \sim \tau_{\gamma\gamma}(E'_{\rm an}) \sim (E'_{\rm an}/E'_{\rm cutoff})^{-1-\beta} \sim (E'_{\rm cutoff}/m_e c^2)^{2(1+\beta)} \gg 1$ (where $\beta < -1$ is the high-energy photon index). This is inconsistent with the observed spectrum and light curve, as mentioned above, since such a large optical depth would thermalize the spectrum and suppress the temporal variability. Alternatively, a high-energy cutoff may reflect the energy spectrum of the accelerated electrons, but it is not clear why a power-law would extend over a very narrow range in this case and a much larger dynamical range in most other cases.

4.2. Comparison to Recent GRBs with High-energy Emission

GRB 080514B was detected by *AGILE*, triggering on board both the Super*AGILE* X-ray detector (SA) and the *AGILE*/ MCAL detector, and was observed by the GRID instrument up to 300 MeV (Giuliani et al. 2008). The gamma-ray data above 30 MeV show a significant extended duration with respect to emission in the hard X-ray and soft gamma-ray energy bands. A detailed analysis of this component was not possible due to limited statistics. Another interesting fact is that in the case of GRB 080514B, some GRID events are detected when the low-energy emission has faded beyond detectability both in MCAL and SA instruments. Similarly, in the case of GRB 080825C, emission in the NaI detectors has receded to background level when the last LAT events are detected. In both cases, the behavior of the high-energy emission in the last part of the prompt emission does not seem to be correlated with that of the low-energy emission. This suggests that it may originate from a physically distinct emission region. The similar behavior observed in the high-energy emission of GRBs 080514B and 080825C may suggest a common explanation.

The longer duration of the high-energy (> 100 MeV) emission relative to the low-energy ($\lesssim 1$ MeV) emission, and to some extent (though with much smaller statistical significance) its later onset, are present not only in GRB 080825C, but also in the two subsequent LAT GRBs, GRB 080916C (Abdo et al. 2009a), and GRB 081024B (Omodei et al. 2008). Therefore, they appear to be common features of at least the first three LAT GRBs. Additionally, the onset of the LAT high-energy emission coincides with the second peak in the GBM low-energy light curve in all these three LAT GRBs. This has led Abdo et al. (2009a) to favor an interpretation in which the first and second spikes of the low-energy light curve originate from two distinct emission regions with different intrinsic emission spectra, where the second spike has a harder high-energy photon index β. This therefore accounts for the LAT detection of the second spike and non-detection of the first spike. This interpretation is further supported in the case of GRB 080916C by the clear change in both the low-energy (α) and high-energy (β) photon indices between the first and second peaks of the GBM (low-energy) light curve. This is not clearly seen in GRB 080825C, possibly since it was not nearly as bright as GRB 080916C. Other explanations for the delayed onset are possible, and several other models were also considered by Abdo et al. (2009a) for GRB 080916C. It was hard to clearly distinguish between the different models on the basis of the available data, despite the extreme brightness of GRB 080916C (which had an extremely large fluence of 2.4×10^{-4} erg cm^{-2} and a record breaking $E_{\gamma,\rm iso}$ of 8.8×10^{54} erg). For GRB 080825C, it is even harder to distinguish between the different possible explanations.

Temporally extended high-energy (> 100 MeV) emission, which lasted longer than the prompt low-energy (sub-MeV) emission, was detected not only in GRB 080825C, but also in the other two LAT GRBs mentioned above (080916C and 081024B), as well as in the *AGILE* GRB 080514B and the EGRET GRB 940217 (Hurley et al. 1994). However, GRB 080825C is the only one so far that shows a hint of a minimum in the high-energy flux between the early and late high-energy emission, which strengthens the case for an origin from a distinct physical region, as discussed above. In GRB 080825C, the late time high-energy emission has a harder photon index than the earlier high-energy emission, which is consistent with an external shock origin. The opposite is true for GRB 080916C,

which favors a somewhat different model such as external Compton scattering of late time X-ray flare photons by forward shock electrons. In GRB 080825C the highest-energy photon was detected after 28 s when the low-energy emission was already down to a very low level, while in GRB 080916C the highest energy photon was detected after 17 s, while the low-energy emission was still very active. Moreover, the observed duration of the high-energy emission in GRB 080825C lasted only slightly longer than the low energy emission (up to ~31 s compared to $T_{90} \sim 27$ s) while in GRB 080916C it lasted much longer (more than $\sim 10^3$ s, compared to $T_{90} = 66$ s). While the high-energy emission in GRB 080916C was detected for a longer time, partly because it was generally much brighter than GRB 080825C, it is also possibly because the flux decayed more slowly at late times (as $t^{-1.2 \pm 0.2}$, compared to steeper than $\sim t^{-1.7}$ in GRB 080825C).

5. CONCLUSIONS

GRB 080825C is the first GRB detected by the LAT, with 13 events above 80 MeV and a detection significance of ~6σ. The highest energy events, up to ~600 MeV, are detected at late times, ~25–35 s after the GBM trigger, when the emission in GBM has decreased close to the background level. The lack of >1 GeV events in the LAT and the large angle of the source to the LAT boresight result in a localization uncertainty of 1°1 (statistical plus systematic) at the 1σ level.

The prompt emission spectrum from both instruments on-board *Fermi* covers over five decades in energy. We have performed time-resolved spectral analysis using the two GBM NaI detectors with the brightest GRB signal, both GBM BGO detectors, and for the LAT with an event selection scheme that is optimized for GRB analysis. We have carefully taken the energy-dependent backgrounds into account for both GBM and LAT, and studied the systematic uncertainties in the spectral analysis. The time-integrated and time-resolved spectra are well fit by the Band function with a hard-to-soft evolution in the first 25 s: E_{peak} evolves from ~300 to ~150 keV, the high-energy power-law index β is constant at a value of ~ -2.5, while the low-energy power-law index α is fairly constant except for the second time bin which contains the first LAT events. In the last time bin, ~25–35 s after the GBM trigger time, the GBM data are barely above background level, and the spectrum is best fit by a single power law with an index of ~ -2 which is significantly harder than the β values of the earlier intervals.

The duration and start time of the late broad peak in the high-energy emission, ~16–31 s after the trigger, suggest that this peak is emitted by the external reverse or forward shocks, rather than by internal dissipation within the GRB outflow (e.g., internal shocks or magnetic reconnection). The relatively fast flux decay after this peak slightly favors a reverse-forward shock "external" Compton origin over a forward shock SSC origin. Although the origin and emission mechanism for this late peak cannot be conclusively determined because of low number statistics (and the lack of observations at X-ray or optical wavelengths, due to the poor GRB localization), the external shock origin is further supported by the change in spectral behavior, in particular of the spectral index, at these late times. Observations of more, brighter GRBs with both GBM and LAT will be able to test this hypothesis.

REFERENCES

Abdo, A. A., et al. 2009a, Science, 323, 1688
Abdo, A. A., et al. 2009b, ApJS, in press
Atwood, W., et al. 2009, ApJ, 697, 1071
Band, D., et al. 1993, ApJ, 413, 281
Band, D. L., et al. 2009, ApJ, 701, 1673
Baring, M. G. 2006, ApJ, 650, 1004
Bouvier, A., et al. 2008, GRB Coordinates Network, 8183, 1
Conrad, J., Botner, O., Hallgren, A., & Perez de Los Heros, C. 2003, Phys. Rev. D, 67, 012002
Cutini, S., et al. 2009, GRB Coordinates Network, 9077, 1
Dingus, B. L. 1995, Ap&SS, 231, 187
Giuliani, A., et al. 2008, A&A, 491, L25
Gonzalez, M., et al. 2003, Nature, 424, 749
Granot, J., Cohen-Tanugi, J., & do Couto e Silva, E. 2008, ApJ, 677, 92
Granot, J., & Guetta, D. 2003, ApJ, 598, L11
Gregory, P. 2005, Bayesian Logical Data Analysis for the Physical Sciences (Cambridge: Cambridge Univ. Press)
Helene, O. 1983, Nucl. Instrum. Methods Phys. Res., 212, 319
Hurley, K., et al. 1994, Nature, 372, 652
Klebesadel, R. W., Strong, I. B., & Roy, A. O. 1973, ApJ, 182, L85
Kouveliotou, C., et al. 1993, ApJ, 413, L101
Li, T., & Ma, Y. 1983, ApJ, 272, 317
Lithwick, Y., & Sari, R. 2001, ApJ, 555, 540
Loredo, T. J. 1992, in Statistical Challenges in Modern Astronomy, ed. E. D. Feigelson & G. J. Babu (New York: Springer), 275
Mattox, J. R., et al. 1996, ApJ, 461, 396
McEnery, J., et al. 2008, GRB Coordinates Network, 8684, 1
McEnery, J., et al. 2009, GRB Coordinates Network, 9044, 1
Meegan, C., et al. 2009, ApJ, 702, 791
Norris, J. P., et al. 1986, Adv. Space Res., 6, 19
Ohno, M., et al. 2009a, GRB Coordinates Network, 8903, 1
Ohno, M., et al. 2009b, GRB Coordinates Network, 9021, 1
Ohno, M., et al. 2009c, GRB Coordinates Network, 9334, 1
Omodei, N., et al. 2008, GRB Coordinates Network, 8407, 1
Omodei, N., et al. 2009, GRB Coordinates Network, 9350, 1
Pe'er, A., & Waxman, E. 2004, ApJ, 603, L1
Rolke, W. A., López, A. M., & Conrad, J. 2005, Nucl. Instrum. Methods Phys. Res., 551, 493
Sari, R. 1997, ApJ, 489, L37
Sari, R., & Esin, A. A. 2001, ApJ, 548, 787
Sommer, M., et al. 1994, ApJ, 422, L63
Tajima, H., et al. 2008, GRB Coordinates Network, 8246, 1
Van der Horst, A. J., et al. 2008, GRB Coordinates Network, 8141, 1
Wang, X. Y., Dai, Z. G., & Lu, T. 2001, ApJ, 556, 1010